Geomorphology 465 (2024) 109401

Contents lists available at ScienceDirect

Geomorphology

journal homepage: www.journals.elsevier.com/geomorphology

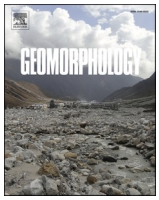

Geomorphological evidence for volcano-tectonic deformation along the unstable western flank of Cumbre Vieja Volcano (La Palma)

Luisa Rollwage [a,*], Olga Sánchez-Guillamón [b], Christian Sippl [c], Ricardo León [d], Juan Tomás Vázquez [b], Morelia Urlaub [a,e], Felix Gross [a,f], Christoph Böttner [a,g], Sebastian Krastel [a], Jacob Geersen [a,h]

[a] Institute of Geosciences, Kiel University, Germany
[b] Spanish Institute of Oceanography, Oceanographic Centre of Málaga (IEO-CSIC), Fuengirola, Spain
[c] Institute of Geophysics, Czech Academy of Sciences, Prague, Czech Republic
[d] Geological and Mining Institute of Spain (IGME-CSIC), Madrid, Spain
[e] Geomar Helmholtz Centre for Ocean Research Kiel, Germany
[f] Center for Ocean and Society, Kiel University, Germany
[g] Department of Geoscience, Aarhus University, Denmark
[h] Leibniz Institute for Baltic Sea Research, Warnemünde, Germany

ARTICLE INFO

Keywords:
Cumbre Vieja volcano
Submarine morphology
Volcano-tectonic deformation
Marine geohazards
La Palma
Canary Islands

ABSTRACT

In 2021, La Palma's southern volcanic complex Cumbre Vieja erupted for its longest period in historic times. Although the geological record shows no evidence for a collapse of Cumbre Vieja, ground deformation studies and field observations suggest that its western flank is moving seawards, following the direction of previous collapses of the island. To better estimate the hazard of a potential flank collapse of Cumbre Vieja, it is important to identify the lateral extent and depth of the mobile sector. Here, we analyse the volcano-tectonic deformation along Cumbre Vieja's western flank, based on geomorphological analysis of combined topographic and new ship-born bathymetric data as well as the analysis of shallow seismicity records associated with the 2021 eruption. In our interpretation, the shoreline-crossing Puerto Naos Ridge results from tectonic uplift accompanying trans-pressional deformation along the northern boundary of Cumbre Vieja's moving flank, therefore decoupling a stable sector in the north from the mobile sector farther south. The proposed moving sector is consistent in scale with previous ground deformation studies and documented flank collapses of structurally similar volcanoes. We present a workflow for semi-automatically detecting boundaries of unstable volcanic flanks based on morphological changes captured in digital elevation data. The method correctly delineated the known boundaries of the unstable flanks of Mt. Etna and Kilauea volcanoes. The ability to constrain potential boundaries of unstable volcanic flanks should inform the planning of future geophysical and geodetic campaigns aiming to identify precursory signals of potential flank failures.

1. Introduction

The interplay between volcanic growth and gravitational deformation has shaped the land-to-sea morphology of the Canary Islands (Figs. 1 and 2). Multiple volcanic flank collapses with an average reoccurrence interval of 125–170 ka altered the morphology of the surrounding deep ocean floor (Urgeles et al., 1999; Krastel et al., 2001; Masson et al., 2002). Over million-year time scales, new volcanic edifices can build upon the remnants of previously collapsed volcanoes and hence the process can be cyclical (Walter and Schmincke, 2002). The huge volumes (up to tens of km^3) and kinetic energies involved in such landslides, and their potential to trigger major tsunamis, represent a destructive geohazard (Paris, 2015). This is evident from the geological record as well as from direct observations including the volcanic eruption and collapse of Anak Krakatau in 2018 (Walter et al., 2019). Flank collapses therefore belong to the greatest natural hazards on Earth (Karstens et al., 2023), and identifying unstable volcanic flanks, including their outline and spatial extent, is essential for estimating the

* Corresponding author.
E-mail address: luisa.rollwage@stu.uni-kiel.de (L. Rollwage).

https://doi.org/10.1016/j.geomorph.2024.109401
Received 21 January 2024; Received in revised form 24 July 2024; Accepted 23 August 2024
Available online 24 August 2024
0169-555X/© 2024 The Authors. Published by Elsevier B.V. This is an open access article under the CC BY-NC-ND license (http://creativecommons.org/licenses/by-nc-nd/4.0/).

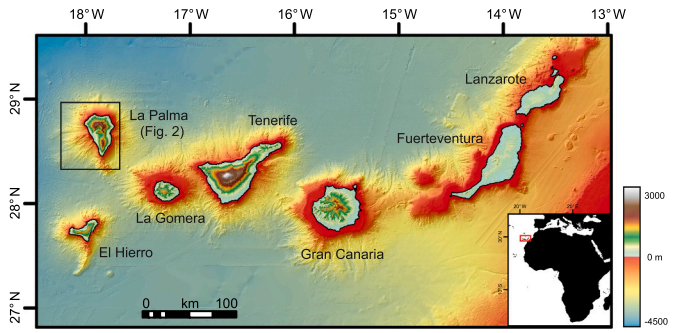

Fig. 1. The Canary Island archipelago from combined topographic and bathymetric data. Inset map shows the location of the Canary Islands west of the African coast. Bathymetric data from the Global Multi-Resolution Topography (GMRT) synthesis (Ryan et al., 2009). Topographic data from the National Geographic Institute (IGN).

hazard potential.

Due to the complex nature of flank motion and limited available instrumental data, the driving mechanisms and timing of flank instability are still poorly understood (Denlinger and Morgan, 2014). Global Navigation Satellite System (GNSS) stations and Interferometric Synthetic Aperture Radar (InSAR) time series data are routinely used to identify and quantify volcanic flank movement in terrestrial areas (e.g. Owen et al., 2000; González et al., 2010; Schaefer et al., 2019). As the largest part of coastal and ocean island volcanoes, however, is underwater (Klein et al., 2023), marine data play an essential role when analysing the structure and dynamics of volcanic flanks. A comprehensive marine monitoring system including seismometers and geodetic measurements has only been installed on a few individual volcanoes including Mt. Etna (Urlaub et al., 2022) and Kilauea volcano (Cervelli et al., 2002; Phillips et al., 2008; Wei et al., 2021). Deformation can also be inferred by identifying the boundaries of moving flanks through geomorphological analysis. As the flank moves along subsurface faults over geologic time-scales, the movement direction and rate in relation to the geometry of the bounding faults can create distinct patterns of surface deformation, which can be recognized in topographic and bathymetric data. The case of Papa'u Seamount, which has been identified as a transpressional bathymetric high resulting from downslope movement of Kilauea's southern flank (Morgan et al., 2003), demonstrates how flank movement deforms the seafloor in a way that can be identified through geomorphological analysis.

Cumbre Vieja, at an altitude of 1950 m, forms the main volcanic

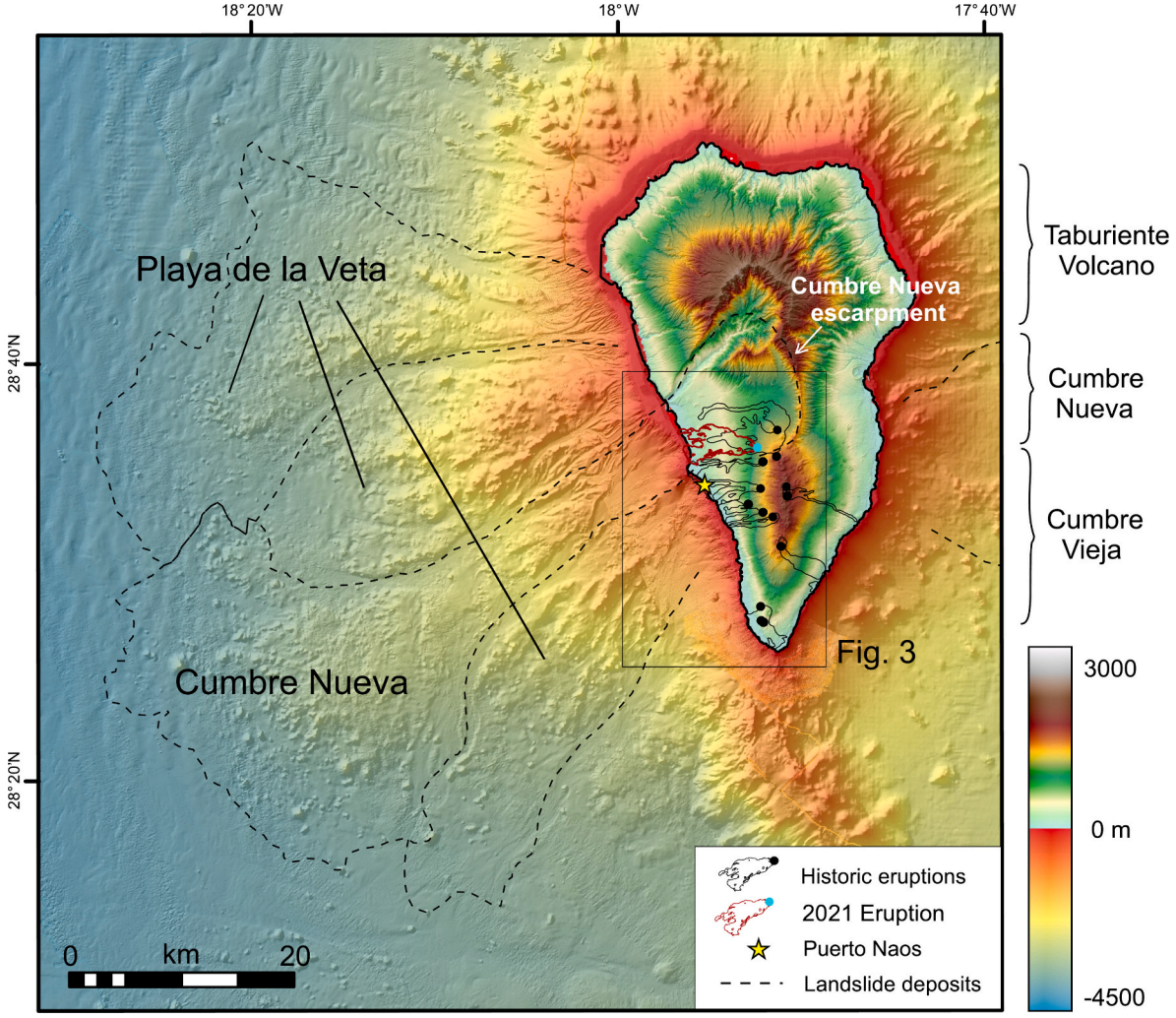

Fig. 2. The land- and seascape of La Palma. The Taburiente-Garafía volcanic complex builds the northern part of the island, while the Cumbre Nueva and Cumbre Vieja ridge extend towards the south. Mass transport deposits at the seafloor indicate collapses of previous volcanoes (Urgeles et al., 1999; Masson et al., 2002). Vents and lava flows of the eruptions in the past 500 years (including the 2021 eruption) concentrated along the crest and the western side of Cumbre Vieja volcano (Fernández et al., 2021). The coastal area around the town of Puerto Naos and La Bombilla is affected by an anomalously high CO_2 concentrations since the 2021 eruption (D'Auria et al., 2023).

system in the southern part of La Palma (Fig. 2). From 19th September until 13th December 2021, Cumbre Vieja experienced its longest eruption in historic times during the built up of the new volcano Tajogaite (e.g. Carracedo et al., 2022; Fernández et al., 2022; González, 2022). Within 12 weeks, >110,000 earthquakes were recorded and local communities were confronted with widespread ash fall and lava flows covering an area of >12 km^2 (Carracedo et al., 2022). Some areas that are about 5 km southwest of the 2021 eruption vents have since been affected by anomalously high atmospheric CO_2 concentrations. This includes the urban areas of Puerto Naos and La Bombilla (Fig. 2), where >1000 people were forced to leave their homes due to high toxic gas concentrations (D'Auria et al., 2023). The attention drawn by the recent eruption has also raised interest in other geohazards, such as from potential flank collapse (González, 2022). The role of eruptive activity as a precursor or consequence of these catastrophic events is not clear, although 9 out of 10 flank collapses from the geological record were associated with volcanic eruptions (Furst et al., 2023). For La Palma, we infer at least four major collapse events from mass transport deposits along the seafloor (Urgeles et al., 1999), while there is no evidence for a previous collapse of Cumbre Vieja. However, InSAR ground deformation analyses and field observations of Cumbre Vieja (e.g. Day et al., 1999; González et al., 2010; Fernández et al., 2021) suggest that its western flank is slowly moving seawards, but the boundaries of the moving sector are poorly constrained.

Here we present a shoreline-crossing morphological analysis of volcano-tectonic deformation of Cumbre Vieja's unstable western flank, including the seafloor of the insular margin down to 4200 m water depth. We aim to identify surface expressions from flank movement through interpretation of a combined high-resolution (5 m) terrestrial digital elevation model (DEM) and new multibeam bathymetric data with a 5–60 m resolution. Morphological features of interest include volcanic cones and structurally continuous topographic highs. For the offshore part of the flank, we add further information from acoustic backscatter data, while we include pre-, *syn*- and post-eruption shallow seismicity for the (terrestrial) analysis. From these data, we identified a potential spatial extent of Cumbre Vieja's moving flank and compare the results with the unstable volcanic flanks of Mt. Etna and Kilauea, where the boundaries of the moving sectors are better constrained.

1.1. Geologic setting of La Palma and Cumbre Vieja volcano

La Palma and El Hierro are the youngest Canary Islands, located at the western end of the island chain (Fig. 1). Together with Tenerife, they present the most active Canary island volcanoes. La Palma is in the earliest and most rapid stage of shield formation and is the fastest growing island in the archipelago (Carracedo et al., 1999a). Its edifice is built on the oceanic crust at about 4000 m water depth and reaches a height of 2400 m above sea level. The island's geologic evolution can be divided into three main phases. First, the formation of the northern shield volcanoes including the Taburiente-Garafía complex (Fig. 2) between 4.0 and 0.44 Ma (Staudigel et al., 1986; Carracedo et al., 2001). Repeated collapses of the northern volcanoes are identified as the Playa de la Veta landslide deposit at the seafloor (Fig. 2), with four bulges representing 2–4 individual collapses (Urgeles et al., 1999). After the magmatic activity focused along a N-S rift zone, the Cumbre Nueva ridge (Fig. 2) developed in the second phase between 0.7 and 0.53 Ma (Ancochea et al., 1994). Its catastrophic collapse is evidenced by a prominent escarpment on land and the youngest landslide seafloor deposit (Masson et al., 2002; Fig. 2).

These collapse-related landslides have mainly been interpreted as debris avalanches with runout lengths up to 80 km. The deposits have a total volume of 750 km^3, which accounts for about 10 % of the present-day volcanic edifice. They are characterized by a blocky morphology with individual blocks reaching kilometre-size (Masson et al., 2002). The deposits are divided by channels, that usually form between the bulges of depositional areas (Urgeles et al., 1999).

The third phase includes the build-up of the Cumbre Vieja volcanic complex (Fig. 2), which is the youngest and currently active volcanic system of La Palma. It started developing at 0.125 Ma, with a cliff-forming phase establishing three rift zones. Subsequent magmatic activity continued along two of these rift zones during the platform-forming phase (Guillou et al., 1998). The past 7 ka were characterized by a reorganization of the stress field of the magma plumbing system towards the N-S rift zone and eruptive activity started concentrating along the N-S rift zone as well as the western flank of the volcano (Day et al., 1999). Volcanic deposits from the historic eruptions in 1470–1492, 1585, 1646, 1677–78, 1712, 1949, 1971 and 2021 have been dated (Fig. 2). Cumbre Vieja has been the most rapidly growing volcano of the Canary Islands (Carracedo et al., 1999a) and presently reaches a height of 1950 m with a steep slope of 20–30° (González et al., 2010). The volcanic ridge is partially covered by basaltic lava flows, mainly at the western side, filling the gullies and other valleys (Fig. 2; Acosta et al., 2005).

1.2. Evidence for instability of Cumbre Vieja's flank

The western flank of the Cumbre Vieja ridge (Figs. 2 and 3) is prone to instability as it overlies the weak deposits of previous collapses, such as the Cumbre Nueva deposits, within the Cumbre Nueva escarpment (Carracedo et al., 1999b; Day et al., 1999; Del Potro and Hürlimann, 2009). The structural reconfiguration and temporal variations in the stress field induced by shallow intrusions may further contribute to weakening of the western flank (Day et al., 1999).

InSAR analyses covering volcanically quiet periods between 1992-2000 and 2003–2008 indicate near-horizontal dislocations of approximately 2.5 mm/a in WNW direction (line of sight) with a modelled surface detachment between 2 and 4 km depth below sea level. The surface projection of the best-fitting fault model constrains the movement to an area near the coastline (Fig. 3; González et al., 2010). These observations fit with a dynamic model in which creeping stress from gravitational loading is a dominant driving mechanism during quiet volcanic periods (González et al., 2010). Later InSAR analysis between 2017 and 2020 showed dip-slip sources of a few mm/a in 2–3 km depth, in the same area where earthquake swarms appeared in October 2017 and in February 2018 (Fig. 3; Fernández et al., 2021). The increasing size of the area affected by these dip-slip sources after the second earthquake swarm, may be a further indicator for tectonic fault activity (Fernández et al., 2021).

The formation of a 4 km long surface rupture below Cumbre Vieja ridge crest during the 1949 eruption (Fig. 3) opened a debate concerning whether it resulted from a change in the local stress field or if it is connected to seaward movement of the mobile flank and thus represents its headwall (Day et al., 1999; Hildenbrand et al., 2003). Further surface fracturing that may be due to flank displacements were observed during the 2021 eruption. A 100 m long E-W oriented eruptive fissure system (Fig. 3; González, 2022) developed in 1–3 km distance from the NNW-SSE main fissure system of the 2021 eruption (Fig. 3).

2. Data and methods

For the morphological analysis we combine high-resolution topographic data of La Palma Island with recently recorded bathymetric data of its western submarine part (from 2015 to 2023). We apply ESRI® ArcGIS tools on the merged digital elevation data to analyse morphological changes on an island-wide scale. For qualitative descriptions and analysis of distinct features we use the individual data sets with their respective highest resolution. For the offshore part, we complement our interpretations with backscatter data and further analyse the shallow seismicity in the western side of Cumbre Vieja between 2017 and 2023.

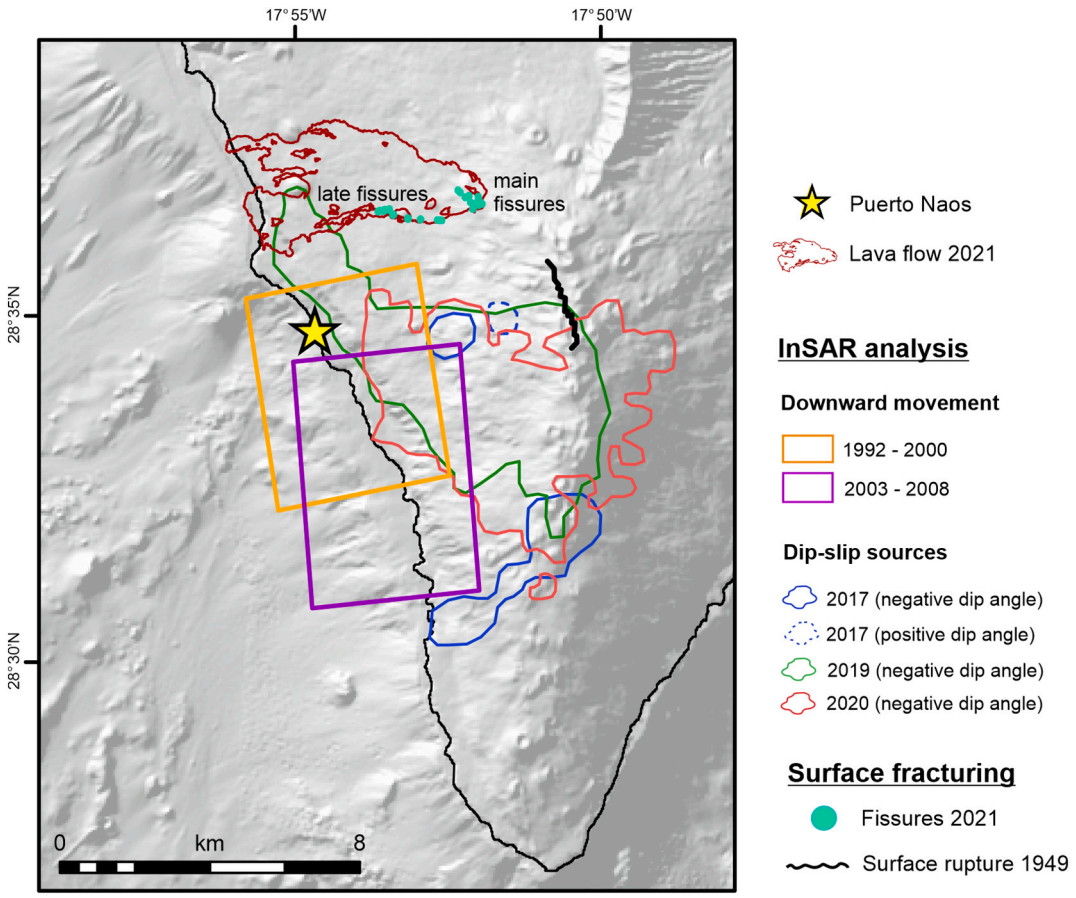

Fig. 3. Evidence for instability of Cumbre Vieja's western flank. The eruption centre and lava flow of the 2021 eruption were on the western side of the Cumbre Vieja volcanic ridge, similar to most of the historical eruptions of the last 500 years (Fig. 2). A 100 m wide late fissure system developed west of the main fissure system of the 2021 eruption (González, 2022). During the 1949 eruption, a 4 km wide surface rupture opened near the volcanic crest (Day et al., 1999; Hildenbrand et al., 2003). InSAR ground deformation studies showed downward movement of the western flank in the volcanically quite periods between 1992-2000 and 2003–2008 (González et al., 2010), as well as dip-slip sources at about 2–3 km depth in the pre-eruption period between 2017 and 2020 (Fernández et al., 2021).

2.1. Topographic data

The topographic data were provided by the National Geographic Institute (IGN; http://centrodedescargas.cnig.es/CentroDescargas/catalogo.do?Serie=LIDAR). The data were recorded with LiDAR flights within the National Aerial Orthophotography Plan (PNOA) in 2009 and gridded to 5 × 5 m.

2.2. Multibeam bathymetry and backscatter data

Multibeam bathymetric data and backscatter data below 1500 m water depth were collected in the framework of the Sub:Palma side user project, which was carried out during R/V Maria S. Merian Cruise 113 between 7-12th January 2023 (Krastel and Cruise Participants, 2024). The data were recorded with an EM122 multibeam system and cover the western flank of La Palma Island (including Cumbre Vieja volcano) from 1500 m water depth down to 4200 m. The data were processed using the software QIMERA and included correcting systematic errors (e.g. applying sound velocity profiles that were recorded during the cruise) and manual editing of the data. After manually deleting single beams with the 3D slice editor, the data were gridded to 60 × 60 m. The backscatter data were subsequently exported from the processed files of the QIMERA project and loaded into the software FMGT to create a backscatter map (mosaic size 40 m).

For shallower water depths above 1500 m, we used multibeam bathymetric data collected by the Spanish Oceanographic Institute (IEO-CSIC) during Vulcana I to III projects. These data were collected between 2015 and 2022 with an EM710 multibeam system during five oceanographic Vulcana Cruises 1015, 0318 and 0921/1021–0222, conducted onboard the Spanish R/V Ángeles Alvariño and Ramón Margalef (Fraile-Nuez et al., 2015, 2021a, 2021b). The bathymetric data were processed with the software CARIS HIPS and SIPS v.11 and gridded to 5 × 5 m and 10 × 10 m.

Bathymetry of surrounding areas was provided by a bathymetric mosaic (90 × 90 m) composed and supplied by the Spanish Navy (Instituto Hidrográfico de la Marina – IHM). The data were collected during the Spanish Economic Exclusive Zone (ZEEE) project and provided to the Spanish Oceanographic Institute under a data transfer license for the purpose of scientific work in the area of La Palma island.

2.3. Mapping spatially continuous topographic highs with drainage divides

Topographic highs were automatically mapped by calculating a drainage system using the ESRI® ArcGIS Hydrology toolset. A drainage system includes drainage pathways that reflect the direction of steepest gradient, analogous to a natural river system. Pour points can be defined at any point along these drainage pathways and relate to areas farther upstream (drainage basins). These basins are bounded by drainage divides that resemble spatially continuous topographic highs.

To calculate a drainage system on an island wide scale, we merged all topographic and bathymetric data at a grid spacing of 90 × 90 m. To prevent discontinuities in the drainage system, the "Fill" tool was used to remove areas with an undefined drainage direction. Based on the filled

data set, the "Flow direction" tool assigns each cell its steepest gradient to one neighbouring cell. The "Flow accumulation" tool then creates a new raster, summarizing the number of cells that are located upstream of each individual cell. In the resulting raster data set, all cells where flow accumulation is zero outline local topographic highs (compare Micallef et al., 2007). By considering only flow accumulation values above a certain threshold (80 in this case), by means of the "Reclassify" tool, we derived spatially continuous drainage pathways (Fig. 4b). To calculate individual drainage divides, we manually provided several pour points in the area of the western flank of La Palma and subsequently applied the "Watershed" tool to calculate the associated drainage divides (Fig. 4d), separating the individual drainage basins.

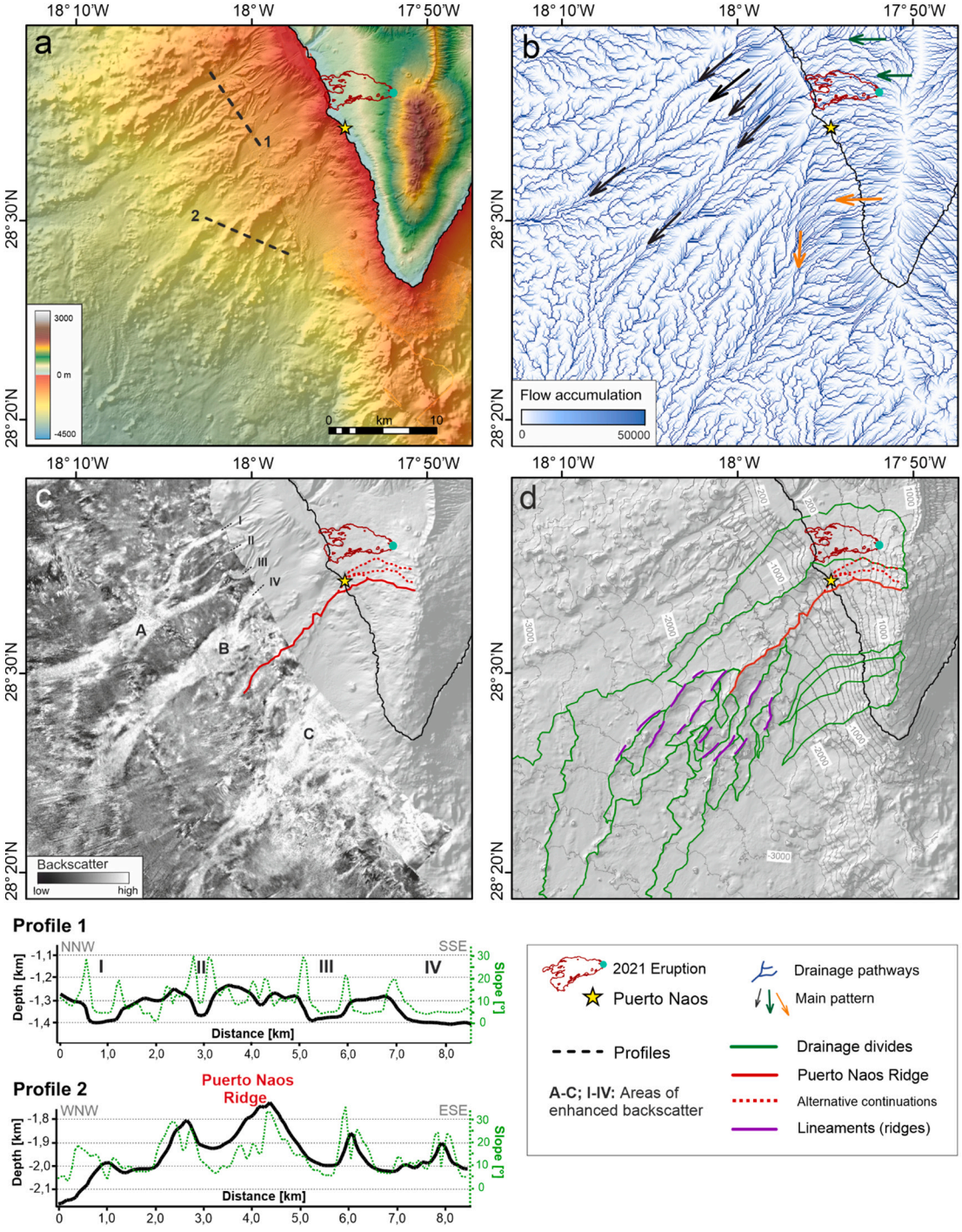

Fig. 4. (a) Topographic data (5 m) combined with bathymetry data derived from Sub:Palma (60 m) and Vulcana cruises (5–10 m). Profiles 1 and 2 located on the map are shown below. (b) Flow accumulation numbers derived from the merged data sets (90 m resolution). Coloured arrows indicate the main flow pattern. (c) Backscatter data from the Sub:Palma project (MSM113) show three large areas of enhanced backscatter values (A, B and C) at the western flank of La Palma and four narrower areas upslope (I, II, III and IV). (d) Drainage divides at the western side of Cumbre Vieja indicate downslope topographic highs (green), including a major shoreline-crossing ridge (Puerto Naos Ridge, highlighted in red) and lineaments formed by ridges of a few kilometres (highlighted in purple). (For interpretation of the references to colour in this figure legend, the reader is referred to the web version of this article.)

2.4. Seismicity

We analysed the earthquake catalogue provided by the National Geographic Institute (https://www.ign.es/web/en/ign/portal/sis-catalogo-terremotos), which is routinely produced for the entire Canary Islands drawing on a network of permanent seismic stations. We filtered the events to restrict feature seismicity to La Palma Island and focused on the period 2017–2023 (Fig. 5). The island's station network has been extended over the years, and consisted of 12 permanent stations at the onset of the 2021 volcanic crisis, during which it was complemented with 5 additional temporary stations (Del Fresno et al., 2023).

For the period 09/2021 to 1/1/2022, we additionally analysed the earthquake catalogue of Del Fresno et al. (2023), who relocated this time segment of the IGN catalogue using a double-difference technique employing waveform correlations. This should yield lower location uncertainties and thus less scatter in the retrieved hypocentre distribution (Fig. 5b).

Unfortunately, neither IGN nor Del Fresno et al. (2023) provide explicit values for location uncertainties. Based on the utilized location methods as well as network geometry, we estimate that onshore events in the IGN catalogue (Fig. 5a, b, panel i-iii) for the investigated time span have absolute location uncertainties on the order of 3 to 5 km, with depths likely being less robust than epicentral coordinates. Del Fresno et al. (2023) (Fig. 5b, panel iv and v) should have obtained much lower relative location errors, likely on the order of 500 m to 1 km.

3. Results

3.1. Drainage divides as downslope trending topographic highs

For the merged topographic and bathymetric data set (90 m resolution), the flow accumulation number on the western side of La Palma ranges from 0 to 50,000 (Fig. 4b). Increasing flow accumulation numbers (from white to blue) outline drainage pathways. Onshore, most

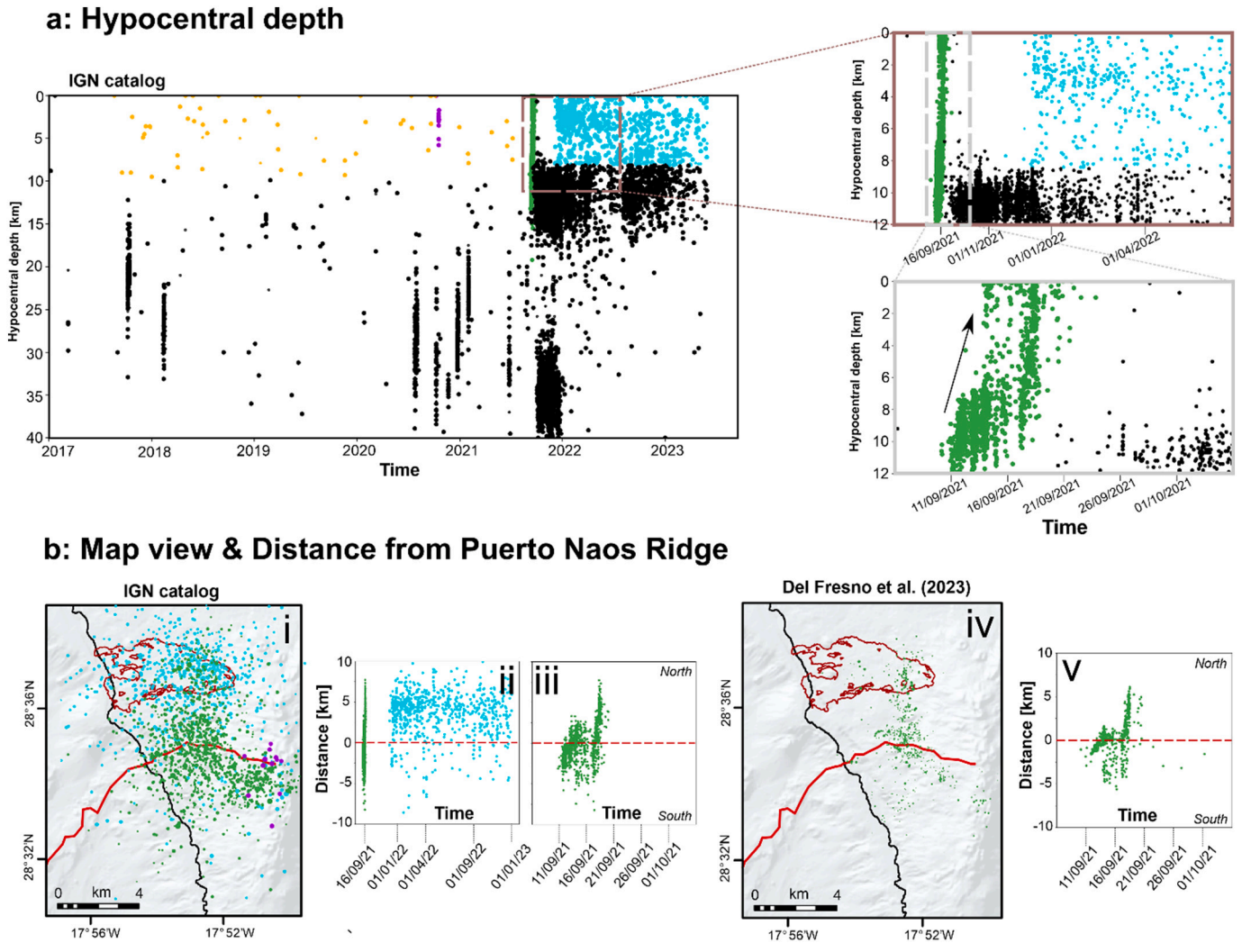

Fig. 5. Time evolution of hypocentral location of seismicity recorded on La Palma Island. (a) Hypocentral depths evolution throughout the years 2017–2023, taken from the IGN catalogue. Orange colours mark scattered, shallow pre-eruption activity, with the short seismicity burst of October 2020 (purple). Green colour marks the initial shallow seismicity preceding the eruption, cyan events show later shallow seismicity from the start of 2022 onwards. Two additional zooms show the 2021/2022 eruption-related seismicity (brown box) as well as the initial phase of seismicity in September 2021 (grey box) in detail. (b) Map view projections of shallow seismicity just before (green) and after (cyan) the 2021 eruption of Cumbre Vieja volcano, for the earthquake catalogue of IGN (panel i) and Del Fresno et al. (2023) (panel iv). The red line marks the position of the Puerto Naos Ridge as determined in this study. Temporal evolution of earthquake hypocentre distances from the ridge for the IGN catalogue (panel ii and iii) and Del Fresno et al. (2023) (panel v). Positive values indicate hypocentres north of the ridge, negative values describe events south of the ridge. The initial phase of seismicity (green) concentrated around the ridge before it migrated northwards shortly before the eruption started. The later more scattered activity (cyan) is centred north of the ridge. (For interpretation of the references to colour in this figure legend, the reader is referred to the web version of this article.)

drainage pathways trend east-west, perpendicular to the crest of Cumbre Vieja (Fig. 4b, green arrows). However, beyond the coastline, the trend directions are different. In the northernmost part of Cumbre Vieja's western flank, dominantly SW-NE trending drainage pathways in the offshore realm (Fig. 4b, black arrows) correlate with the channels that formed between the bulges of landslide deposits at the seafloor (Fig. 4a; Urgeles et al., 1999). The flow pattern changes farther south, towards the central western flank of Cumbre Vieja. Just south of Puerto Naos (Fig. 4b, yellow star), and about 10 km from the coastline, a high number of narrow adjoining drainage pathways change their orientation from E-W to N-S (Fig. 4b, orange arrows). Farther seaward, three SW-NE trending areas with low flow accumulation numbers (Fig. 4b) correspond to drainage divides (topographic highs) that are a few kilometres up to several kilometres long (Fig. 4d, green lines). The drainage divides are mainly SW-NE oriented in the marine environment, while some major shoreline-crossing divides continue onshore with a W-E orientation (Fig. 4d, green lines). One of these major topographic highs (Fig. 4d, red line) crosses the shoreline near the town of Puerto Naos (Fig. 4d, yellow star). With a total length of approximately 30 km, it extends from the crest of Cumbre Vieja down to a water depth of 2000 m. This ridge changes orientation from W-E on land, to SSW-NNE in the shallow water area and to SW-NE between 1500 m down to 2000 m water depth (Fig. 4d). Due to the complex topography near the coast, we also identified two alternative onshore continuations (Fig. 4d, dashed red lines), based on additional pour points that we defined at the coastline. In the offshore part, the ridge is about 150 m higher than the surrounding area (Profile 2) and its height decreases in the onshore direction. The drainage divides (Fig. 4d, green lines) further indicate several smaller (2–4 km long), linear and mainly SW-NE oriented ridges at the seafloor in water depths between 1500 and 3000 m (Fig. 4d, purple lines), concentrating in the southwestern area of the major shoreline-crossing ridge (Fig. 4d, red line). Some WSW-ENE aligned drainage divides of about 20 km length cross the shoreline in the southern part of Cumbre Vieja (Fig. 4d, green lines).

3.2. Backscatter data and profiles

Enhanced backscatter exists in three large SW-NE trending areas along the western slope of La Palma (marked A, B and C in Fig. 4c). The backscatter pattern differs between the northern and the southern part of Cumbre Vieja's western flank, coinciding with the different drainage patterns in the two areas (Fig. 4b). Four bands of high backscatter occur within valleys along the northern flank (marked I, II, III and IV in Fig. 4c). These coincide with downslope trending drainage pathways (Fig. 4b) that outline the channel systems (Fig. 4a, Urgeles et al., 1999). These high backscatter bands are shown by Profile 1 to occur over 200–900 m-wide valleys in the upper slope, morphologically characterized by sharp edges along the thalweg and to the surrounding terrain (marked I, II, III and IV in Profile 1, Fig. 4). These channels amalgamate farther downslope, forming the two northern NE-SW trending high backscatter areas (marked A and B in Fig. 4c). Along their entire course, these northern valleys show a sharp backscatter contrast to their surroundings. In the central and the southern part of the offshore volcano flank (between area B and C), the valleys are not marked by such distinctive contrasts in backscatter (Fig. 4c and Profile 2). This is the area where we identified the major drainage divides and several smaller lineaments formed by ridges (Fig. 4d). Backscatter values along the valleys seem to be overall reduced compared to the backscatter in areas A, B and C (Fig. 4d). Backscatter from inter-valley ridges (Fig. 4d, red and purple lines) also appears more heterogeneous. Profile 2 (Fig. 4a) shows the relief and slope across the linear ridges, revealing that the valleys between the ridges are bounded by a smoother morphology compared to the valleys in Profile 1 (Fig. 4a).

3.3. Seismicity

Between 2017 and September 2021, a total of 7 short-duration seismic swarms (Fig. 5a, black dots) occurred at depths between 15 and 35 km. Shallow seismicity during this time interval (Fig. 5a, orange dots) was very sparse, with the one exception of a short seismicity burst of 12 events within <24 h on 18th October 2020 (Fig. 5a, purple dots). The seismicity signature of the 2021 eruption has been described by many authors (e.g. D'Auria et al., 2022; Dayton et al., 2023; Del Fresno et al., 2023). Before the eruption started, seismicity was confined to the uppermost ~12 km and migrated to shallower depths until the eruption onset on 19th September 2021 (Fig. 5a, lower right zoom, green dots). After this time, two clusters of seismicity at ~8–16 and ~30–40 km depth (Fig. 5a, black dots) were persistently active beyond the duration of the eruption, whereas shallower seismicity was absent. Shallower events returned around the start of 2022 (Fig. 5a, upper left zoom, cyan dots), which was not reported in the aforementioned studies due to their limited time interval of analysis.

In the following, we focus on shallow seismicity (depth < 10 km) and largely disregard the two most prominent clusters that were active at deeper depth during the 2021 eruption. When plotted together with the Puerto Naos Ridge (Fig. 5b), both the initial shallow seismicity episode from 11th to 19th September 2021 (Fig. 5b, green dots) and the later returning shallow seismicity around the start of 2022 (Fig. 5b, cyan dots) occur within a few kilometres of the ridge. The former started around the ridge (+−2.5 km horizontal distance), then migrated northwards to a location 5–7.5 km north of the ridge (Fig. 5b, panel iii and v, green dots), while hypocentral depths got successively shallower (Fig. 5a, lower right zoom, green dots). The later activity is much more scattered and appears to be centred north of the ridge, not showing any sign of temporal migration (Fig. 5b, panel ii, cyan dots).

4. Discussion

We identified a spatially continuous shoreline-crossing morphological ridge, hereafter referred to as the Puerto Naos Ridge, trending downslope the western flank of Cumbre Vieja volcano. Puerto Naos Ridge acts as a major drainage divide (topographic high) from the top of the volcano to the abyssal seafloor (Figs. 6a and 7, red line). We interpret this feature as the surface expression of the lateral boundary of the moving flank, separating a stable section to the north from an unstable section to the south. In our conceptual model of volcano-tectonic deformation, the ridge results from localized tectonic uplift due to transpressional deformation along the boundary of Cumbre Vieja's moving flank. This interpretation is based on the arguments outlined below.

4.1. Flank-bounding shallow crustal faults as fluid conduits

In the suggested tectonic model, crustal faults possibly accommodate transpressional deformation along the northern boundary of Cumbre Vieja's moving flank, and thus form Puerto Naos Ridge. Branching of these faults at shallow depth may explain the multitude of often parallel aligned lineaments that appear as 2–4 km long ridges between 1500 and 3000 m water depth (Figs. 6a and 7, purple lines). A similar tectonic setting with transpressional faults branching at shallow crustal levels resulting in downslope bathymetric scarps and ridges is proposed for Papa'u seamount, which represents the boundary of the southern moving flank of Kilauea volcano (Fig. 8; Morgan et al., 2003).

As magma in dykes favours areas of high stress (e.g. Watanabe et al., 2002; Menand et al., 2010; Maccaferri et al., 2019; Pinel et al., 2022), the presence of such compressional regimes also supports the hypothesis of magma migration in the area around Puerto Naos Ridge. Some local topographic highs that may resemble submarine volcanic cones (Fig. 6a-e, black circles, marked yellow in Fig. 6d and e) extend to the mid-slope region around 700 m water depth. This observation, together with a

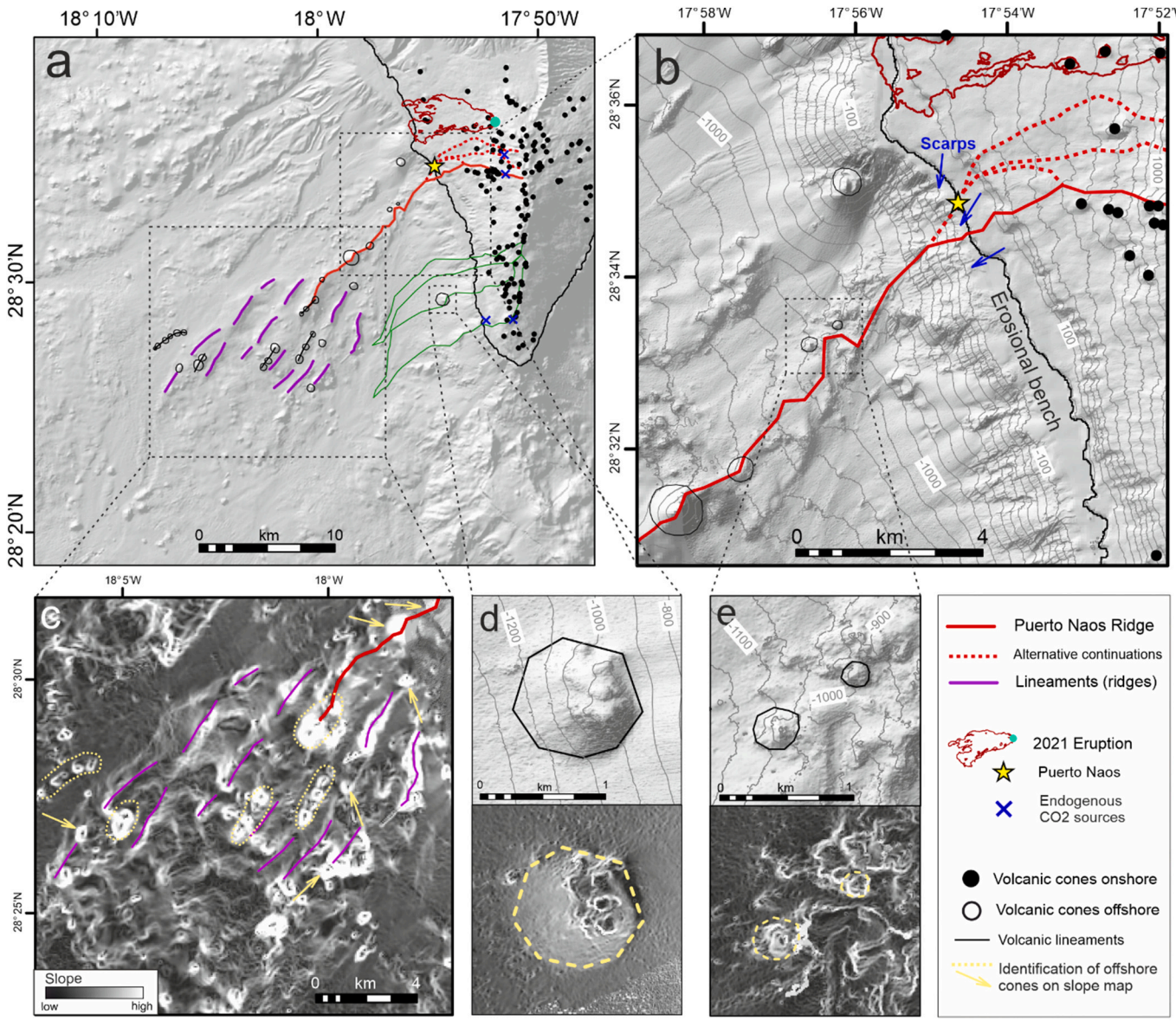

Fig. 6. (a) Puerto Naos Ridge (red line) and alternative onshore continuations (dashed red lines) due to the complex topography around the coastline. Smaller ridges (purple) form lineaments at the seafloor. Submarine near-circular hills (black circles), here interpreted as volcanic cones, as well as cones on land (black dots; Carracedo et al., 2015) populate the western flank of Cumbre Vieja. Enhanced endogenous CO_2 concentrations were measured in Puerto Naos (yellow star) since the 2021 eruption (D'Auria et al., 2023) and at four other sites in 2002 (blue crosses; Padrón et al., 2015). (b) Zoom on land-to-sea-transition showing the erosional bench, which is incised by several scarps. (c) Enlarged slope map of the mid-slope region showing local topographic highs (yellow) that are similarly aligned to the ridges (red and purple) and therefore may be of volcanic origin. (d) and (e) Zooms on local topographic highs near Puerto Naos Ridge that resemble volcanic cones showing their shaded relief (upper panel) and surface slope (lower panel). (For interpretation of the references to colour in this figure legend, the reader is referred to the web version of this article.)

multitude of cones close to the onshore ridge (Fig. 6a and b, black dots; Carracedo et al., 2015), indicates the likely presence of shallow crustal faults that guide magma at crustal levels to the seafloor. As such faults often accommodate aligned vents and craters (Hunt et al., 2019), some local topographic highs (Fig. 6a, black circles and lines; marked yellow in Fig. 6c) that are similarly aligned as the potential fault outcrops (purple lines) may also represent volcanic cones. Magma dykes can also contribute to flank mobilization (Thiele et al., 2023). This may also be relevant, particularly around the onshore continuation of Puerto Naos Ridge.

The coastal area around the town of Puerto Naos (Fig. 6a) is affected by high CO_2 concentrations almost three years after the eruption (D'Auria et al., 2023). The sources and migration pathways of the CO_2 remained unknown. Since Puerto Naos is in the area where Puerto Naos Ridge intersects the coastline (Figs. 6a and 7), it seems possible that upward CO_2 migration along transpressional faults from flank movement govern the intense degassing in this area. Previous CO_2 efflux surveys were acquired to analyse CO_2 accumulation at Cumbre Vieja between 2001 and 2013 (Padrón et al., 2015). Samples from 2002 revealed four sites of primary endogenous CO_2 origin (Fig. 6a, blue crosses), suggesting a deeper origin (Padrón et al., 2015). Diffusive CO_2 emission along crustal faults is known from other active volcanoes such as Unzen volcano (Ohsawa et al., 2002) and Miyake-jima volcano in Japan (Hernández et al., 2001).

From the available data, and due to the lack of deep penetrating seismic reflection lines, we are unable to resolve the thickness of the moving sector and hence the depth and nature of the basal detachment. For Kilauea volcano (Hawaii), for example (Fig. 8), volcano-tectonic

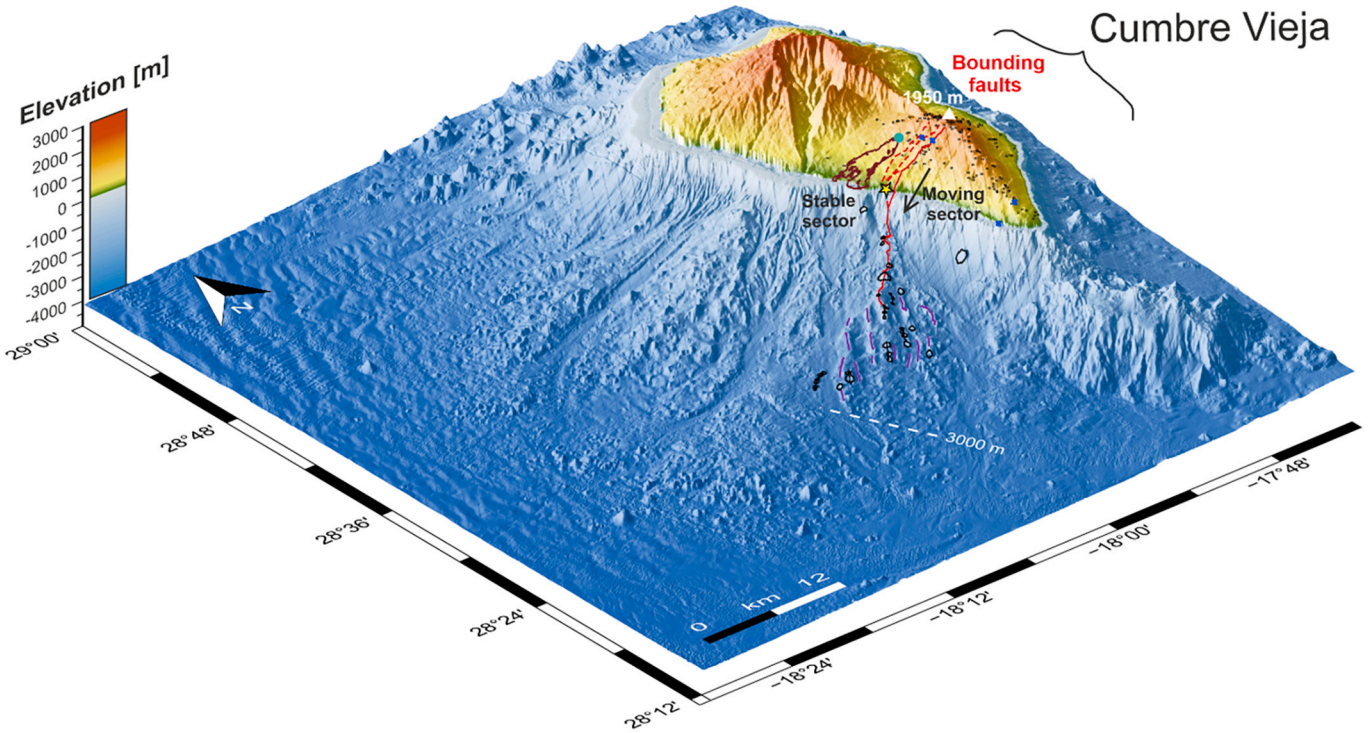

Fig. 7. Perspective view of La Palma Island summarizing the main geomorphological interpretations of this study regarding the volcano-tectonic deformation of Cumbre Vieja's western flank. We interpret Puerto Naos Ridge as the northern boundary of Cumbre Vieja's moving flank. The ridge results from localized uplift due to transpressional deformation and therefore divides a stable sector to its north, form a seaward (westward) moving sector to its south. Potential volcanic cones as well as sites of anomalous CO_2 indicate subsurface faults that guide magma and CO_2 to the surface and accommodate the transpressional deformation. Branching of these faults may result in lineaments at the seafloor at the distal part of the flank down to 3000 m water depth. See legend of Fig. 6 for meaning of different symbols.

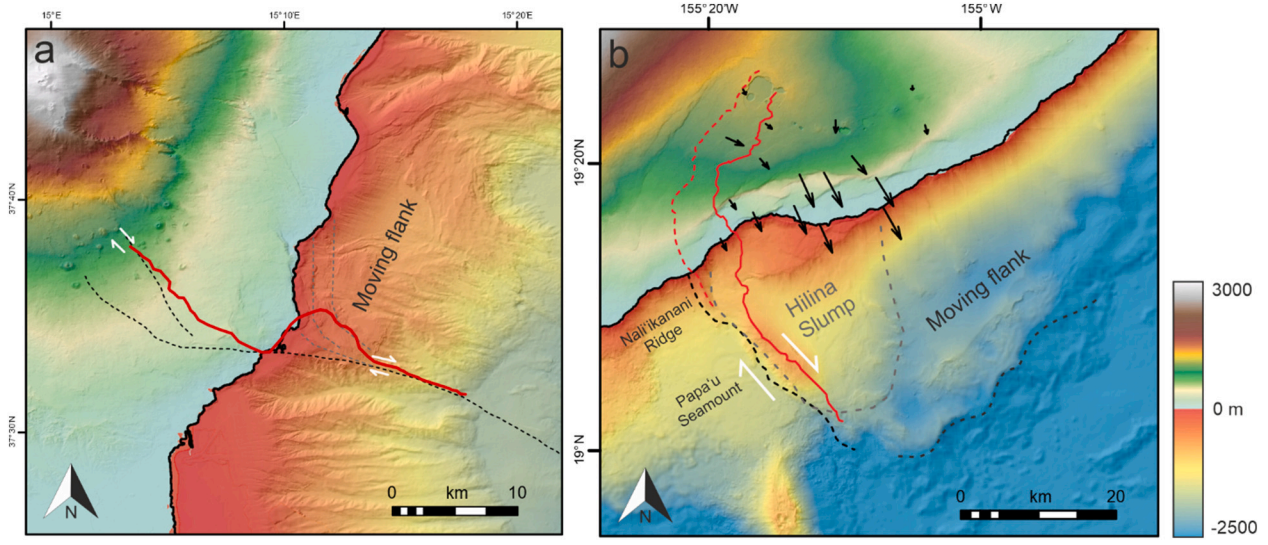

Fig. 8. Moving flanks of (a) Mt. Etna (Sicily), bathymetry data from Gutscher et al. (2017) merged with topographic data from SRTM15+ grid (Becker et al., 2009), and (b) Kilauea (Hawaii), data from the Global Multi-Resolution Topography (GMRT) synthesis (Ryan et al., 2009). Drainage divides (red lines) align with the topographic highs, that are associated with the bounding faults (dashed black lines; Morgan et al., 2003; Gross et al., 2016; Urlaub et al., 2022). White arrows show the strike-slip movement along the bounding faults, black arrows show the onshore moving direction of Kilauea's flank from GNSS stations (Poland et al., 2017). (For interpretation of the references to colour in this figure legend, the reader is referred to the web version of this article.)

models suggest that its southern flank moves along a décollement consisting of volcanic pile and weak pelagic clay in about 8 km depth at the interface to the underlying oceanic crust (Denlinger and Okubo, 1995; Morgan et al., 2000; Morgan et al., 2003; Denlinger and Morgan, 2014). A shallower slump (Hilina slump) with a detachment in the primary volcanic edifice in about 3–5 km depth is further activated during larger earthquakes (Morgan et al., 2003; Lin and Okubo, 2020). Both sliding mechanisms are probably part of the transpressional deformation of Papa'u Seamount. Cumbre Vieja was built on the weak debris avalanche deposits of the Cumbre Nueva collapse, which overly the remnants of the northern shield volcanoes (Carracedo et al., 1999b; Day et al., 1999). InSAR ground deformation modelling suggested a basal detachment of

the moving sectors between 2 and 3 km depth for the dip-slip sources between 2017 and 2020 (Fernández et al., 2021) and 2–4 km near the coast during the volcanically quiet periods between 1992–2000 and 2003–2008 (González et al., 2010). A sliding detachment at the base of the Cumbre Nueva collapse deposits or even deeper at the volcanic basement would explain a low-density body inferred from gravity modelling (Camacho et al., 2009; González et al., 2010). As gravity models are non-unique, the low-density anomaly might also result from tectonic extension due to the downward moving flank. A detachment surface at such depth would also explain the several adjacent ridges between 1500 and 3000 m water depth (Figs. 6a and 7, purple lines) as wide branches of crustal faults. However, the example of the Hilina Slump at Kilauea (Fig. 8) shows that unstable volcanic flanks can accommodate more than one detachment fault (Morgan et al., 2003), and thus it cannot be ruled out that Cumbre Vieja's flank is also moving somewhere at shallower crustal levels.

4.2. Permanent geologic deformation resulting from flank movement

Tectonic faults accommodate transpressional deformation from flank movement, thereby altering marine and terrestrial morphology and guiding drainage patterns on an island-wide scale, including the newly interpreted Puerto Naos Ridge (Figs. 6a and 7, red line). Geological and anthropogenic processes such as lava flows, volcanism, anthropogenic land use or construction modify relief on limited spatial scales, affecting the drainage patterns in their vicinity. The continuation of a structural feature such as Puerto Naos Ridge across different geologic domains (from the crest, across the coast down to the midslope region), together with a predominant linear orientation, suggests a tectonic origin. The exact trend of the ridge across the shoreline cannot be reliably determined. In its vicinity, the erosional bench (Fig. 6b), which relates to the last glacial maximum, is shaped by scarps and lineaments that may result from tectonic deformation (compare Quartau et al., 2010; Mitchell et al., 2012; Quartau et al., 2015). In this area, however, erosion by lava flows or landslides as well as vast anthropogenic alteration overprints pristine tectonic morphology. This implies a high degree of uncertainty related to the interpretation of the nature of any morphologic features in this area. We therefore derived several alternative terrestrial continuations of the ridge (Figs. 6a and 7, dashed red lines) by defining pour points at the coastline and calculating upslope drainage divides. Lava flows from the 1585 Tajuya eruption and the 1949 Llano del Banco eruption (Fig. 2; Fernández et al., 2021) also form downslope topographic highs in this area. However, as the drainage divides only partially correlate with the lava flows related to the 1585 and 1949 eruptions, they appear to have a deeper tectonic origin. The northernmost drainage divide also coincides with the southernmost fault deformation band inferred from the 2021 eruption-related seismicity distribution and previous surface fractures (compare Fig. 13, Rodríguez-Pascua et al., 2024). The two southern onshore continuations of the Puerto Naos Ridge coincide with the two northern 2002 sample sites showing enhanced endogenous CO_2 concentrations (Figs. 6a and 7; Padrón et al., 2015), supporting our structural interpretation of underlying transpressional faults guiding CO_2 to the surface, analogous to the coastal area around Puerto Naos.

As the Canary Islands all have a similar structural setting (e.g. Mitchell et al., 2002; Carracedo, 1994), we would expect that previous flank collapses acted on similar spatial scales. The El Golfo collapse on El Hierro affected the volcano from its crest down to water depths of 3200 m (Urgeles et al., 1997). The remaining amphitheatre-shaped headwall reaches a height of 1500 m and the distance between the lateral boundaries ranges from 14.5 km at the top to about 21 km at the most distal submarine part. The data presented here indicate that the unstable sector of Cumbre Vieja may cover a similar area in both distal and proximal directions. The most distal part of the linear ridges (Figs. 6a and 7, purple lines) associated with underlying crustal scale faults reaches a water depth of about 3000 m (Fig. 7, dashed white line).

The partly linear structure and oblique orientation of Puerto Naos Ridge to the depth contour lines (Figs. 4d, 6b), argues against a sedimentary origin of the ridge. Based on the following arguments, we suggest that this ridge is primarily formed by tectonic uplift and partly shaped by erosional processes. Backscattering changes with geometry and material composition of the seafloor thus indicating geological structures and related processes. From the backscatter data (Fig. 4c), we infer that Puerto Naos Ridge separates two active sedimentary regimes. High backscatter values towards the NW (marked B in Fig. 4c) and SE (marked C in Fig. 4c) indicate coarse-grained material, that possibly results from active erosion exposing the hard volcanic seafloor or deposition of sands and gravel from sediment flows. The heterogeneous backscatter pattern around the area of Puerto Naos Ridge (between B and C in Fig. 4c) possibly results from geometrical effects of the ridges (lower backscatter) in combination with erosion or deposition of sediment flow (higher backscatter), that might also overtop the ridges. We would expect gravitational erosion from downslope currents to remove or overprint the ridge over geological time, particularly above 1500 m water depth, where Puerto Naos Ridge is oblique to the depth contour lines (not covered by the backscatter data) (Fig. 6b). The fact that it is withstanding these processes points towards *syn*-erosional uplift of the ridge that is outpacing its erosion by gravity flows. Below 1500 m water depth, sediment flow seemed to be partially guided by the inter-channel ridges. Their morphology and backscatter contrast, however, differ from the northern channels outside of the area affected by the moving flank (marked I, II, III and IV in Fig. 4c and Profile 1). While the morphologically distinct northern channels seemed to be formed by incision of gravity flow, the heterogeneous backscatter values and smoother morphology of the valleys and ridges in the south (Fig. 4, Profile 2) indicate syn-erosional uplift.

4.3. Linking short-term measurements to permanent geologic deformation

Our interpretation of persistent volcano-tectonic deformation is consistent with short-term deformation measurements over the last two decades with respect to the spatial scale and magnitude of flank deformation. InSAR measurements (Fig. 3; González et al., 2010; Fernández et al., 2021) suggest dislocation sources just south of Puerto Naos Ridge (Figs. 6a and 7, red line) in the area where we interpret the moving sector of the volcano flank based on geomorphological analysis. A deformation of 2.5 mm/a was measured for an area of approximately 40 km^2 near the coast during the volcanically quiet periods between 1992 and 2003 (Fig. 3, orange rectangle) and 2003–2008 (Fig. 3, purple rectangle). Such low deformation rates, together with the absence of eruptive activity and the lack of widespread seismicity indicate creeping stress resulting from gravitational spreading as the dominant driving force (González et al., 2010). Gravitational driving mechanisms usually lead to higher deformation rates in the distal part of the flank, which explains the more distinct shape of Puerto Naos Ridge in the marine part, with respect to its height and lateral extent (Fig. 4, Profile 2). The area covered by the dip-slip sources between 2017 and 2020 (Fig. 3; Fernández et al., 2021) stretches from near the coast to the crest of Cumbre Vieja, again matching with the moving sector from our volcano-tectonic interpretation. The deformation rates were estimated to about a few mm/a, while the increasing area of the dip-slip source after the earthquake swarm in 2018 (Fernández et al., 2021) possibly relates to opening of new fractures associated with flank mobilization.

At present, Puerto Naos Ridge is about 150 m higher than the surrounding area (Fig. 4, Profile 2). Vertical uplift is likely smaller compared to the total displacement along the detachment, as the movement in the subsurface splits up into several faults. Assuming subsurface faults are 45° inclined, a movement rate of about 1.7 mm/a had been required to form Puerto Naos Ridge over 125 years. This is in the same order as the deformation rates of a few mm/a, calculated from InSAR data (González et al., 2010; Fernández et al., 2021). However, the displacement rate measured today is likely to be higher than the average

rate, as a certain period of time has probably elapsed before the volcanic flank started to slide, and displacements have probably increased in magnitude and size during growth of the edifice, up to the displacement rates determined by the recent InSAR studies. On the other hand, magmatic intrusions can lead to episodic acceleration (slow slip events), as observed at Mt. Etna (Palano et al., 2022), while the example of Kilauea shows that large earthquakes can also induce displacements in metres per second (Liu et al., 2018). No large displacements were reported during the 2021 eruption. It is therefore not clear if and how magmatic intrusions and large earthquakes activate flank movement at Cumbre Vieja.

The temporal and spatial trend of the shallow seismicity (<12 km) between 2017 and 2023 (Fig. 5) indicates structural weak zones that potentially connect to the moving flank. The seismicity between 2017 and the start of the eruption shows one significant shallow burst (0–7 km) in October 2020 (Fig. 5a, purple dots) with epicentres concentrating at the top area and south of Puerto Naos Ridge (Fig. 5b, purple dots). The shallow depth together with the location and the short temporal separation may be explained by fault activity connected to the moving flank. Most of the pre-eruptive seismicity in the two weeks prior to the eruption start on 19th September 2021 (Fig. 5, green dots) likely relates to magma ascending from the magma storage reservoirs to the 2021 eruptive centre, while some earthquakes farther south are related to ascending hydrothermal fluids (D'Auria et al., 2022; Cabrera-Pérez et al., 2023). Magma and hydrothermal fluids usually ascend through faults in the subsurface. Despite the location uncertainty, most of this phase of seismicity appears to be located on a south-dipping, planar structure (Cabrera-Pérez et al., 2023). That could be taken as evidence of an inclined fault plane in this region associated with the northern boundary of Cumbre Vieja's moving flank, while the hydrothermal circulation south of Puerto Naos Ridge also indicates weak zones (Heap et al., 2021) that could be related to the moving flank. The absence of shallow seismicity during the 2021 eruption and the sudden reoccurrence after the end of the eruption (Fig. 5a, cyan dots), with a temporal constant concentration north of the Puerto Naos Ridge (Fig. 5b, cyan dots), could be explained by hydrothermal circulation within active faults that has been induced by the magma.

4.4. Lateral extent of the moving sector and potential southern boundary of the moving flank

The seaward movement between 1992 and 2000 (Fig. 3, orange rectangle; González et al., 2010) constrains an area near the coast that has a similar southern extent as the shallow seismicity in the early eruptive period (Fig. 5b, green dots). The 2003–2008 movement (Fig. 3, purple rectangle; González et al., 2010) extends farther south, to a similar extent as the 2017–2020 dip-slip sources (Fig. 3, blue, green and red outline; Fernández et al., 2021). For the second larger extent, we identified three distinct shoreline-crossing topographic highs at Cumbre Vieja's southern end, each of which correlates with a drainage divide (Fig. 6a, green lines). On land, multiple volcanic cones in the vicinity may indicate magma ascent through underlying faults similar to the onshore continuations of Puerto Naos Ridge. One of the offshore continuations (Fig. 4d, green line) also crosses a single volcanic cone (Fig. 6a and d, black circle). Another drainage divide farther south (Fig. 6a, green line) crosses the two southern endogenous CO_2 sites measured in 2002 (Fig. 6a, blue crosses; Padrón et al., 2015), again pointing towards fractures that might connect to the unstable flank.

Overall, the potential boundaries of the moving flank (north and south) (Fig. 6a) indicate a lateral extent between 7 and 10 km. Comparing this again with the island of El Hierro, the El Golfo collapse affected a similar but slightly smaller area, with a diameter of 14.5 km at the top.

4.5. Proof of concept: constraining unstable volcanic flanks through drainage divides

Based on geomorphological analysis, we interpret Puerto Naos Ridge to result from localized uplift due to volcano-tectonic deformation (transpression) at the northern boundary of Cumbre Vieja's moving flank. The spatial alignment of the ridge with a drainage divide, enabled us to explore its shoreline-crossing extent. We therefore assume that surface deformation from flank movement can be distinct enough to produce divides in an island-wide drainage system. To test this hypothesis, we applied our method to Mt. Etna and Kilauea volcano, where the boundaries of the moving flanks are well constrained (Fig. 8). For both volcanoes, the calculated drainage divides (Fig. 8, red lines) largely coincide with the bounding faults of their unstable flanks (Fig. 8, dashed black lines). For Mt. Etna, the southern boundary of the moving flank is well-known from terrestrial and offshore geodetic measurements (Azzaro et al., 2013; Gross et al., 2016; Urlaub et al., 2022). Although the derived shoreline-crossing drainage divide is deflected near the coast by other fault systems (Fig. 8a, dashed grey lines), elsewhere it correlates with the location and trend of the flank bounding fault (Fig. 8a, dashed black line). At Kilauea, the 10 km wide Papa'u Seamount and the Nali'ikakani Ridge define the southwestern boundary of Kilauea's moving flank (Fig. 8b, dashed black line) as well as the boundary of the shallower Hilina Slump (Fig. 8b, dashed grey line; Morgan et al., 2003). Due to the southeastward movement of the flank (Fig. 8b, black arrows; Poland et al., 2017), which is slightly oblique to the western boundary fault (Fig. 8b, dashed black line), the crest of the seamount is a few hundred meters northeast of the bounding fault (Fig. 8b). Consequently, the drainage divide does not coincide exactly with the bounding fault, but rather with the crest of the seamount, which is associated with the fault. Analogous to Cumbre Vieja, we calculated a second alternative drainage divide (Fig. 8b, dashed red line) that follows the nearshore Nali'ikakani Ridge towards the onshore part of the flank. This ridge has a similar origin to Papa'u Seamount (Morgan et al., 2003), but is on the opposite side (west) of the bounding fault. Due to this shift along the depth contour lines, these ridges cannot be traced by one drainage divide. The alternative onshore continuation seems to be more consistent with the onshore flank movement, inferred from GNSS stations (Fig. 8b, black arrows).

Together, the morphological analyses of Cumbre Vieja, Mt. Etna, and Kilauea volcanoes show that volcano-tectonic deformation from flank movement alters the land- and seascape substantially, and is generated sufficiently rapidly, to produce persistent divides in the drainage system on an island-wide scale. This method can therefore be easily applied to constrain potential boundaries of other unstable volcanic flanks. It further emphasizes that one drainage divide is able to trace a shoreline-crossing bounding fault, but alternative continuations based on local morphological variations need to be considered as well.

5. Conclusions

From geomorphological analysis of the combined topographic and bathymetric data, and the spatial and temporal evolution of the shallow seismicity associated with the 2021 eruption, we developed a conceptual volcano-tectonic model for the unstable western flank of Cumbre Vieja. In our interpretation, the large and shoreline-crossing, mainly SW-NE oriented Puerto Naos Ridge results from transpressional deformation and related uplift along the northern boundary of Cumbre Vieja's moving flank. The often localized eruptions of the past 500 years and the recent seismicity at the western flank of Cumbre Vieja indicate zones of structural weakness that provide magmatic pathways at crustal levels and that likely support mobilization of the western flank. Along the onshore continuation of Puerto Naos Ridge, a higher density of volcanic cones compared to the surrounding terrain, and a few sites of anomalously high CO_2 emissions support the presence of shallow crustal faults that guide magma and CO_2 to the surface. Lineaments at the seafloor

may result from branching of the transpressional faults at shallow depths, while a few submarine topographic highs in the vicinity resembling volcanic cones, also suggest magma migration through underlying faults. The spatial evolution of the pre-eruptive shallow seismicity in 2021 suggests a south-dipping fault plane below Puerto Naos Ridge as well as zones of structural weakness farther south, within the area of the proposed moving sector. The related internal structure and dynamics, explaining the observed deformation of the land- and seascape, are consistent with previous ground deformation measurements at Cumbre Vieja's western flank as well as with the shallow seismicity records. The suggested size of this moving sector is similar to known sector collapses from structurally similar volcanoes, such as the El Golfo collapse at El Hierro.

Finally, we developed a method for semi-automatically tracing the bounding faults of unstable volcanic flanks, as they often correlate with shoreline-crossing, spatially continuous topographic highs. We identified these topographic highs by calculating an island-wide drainage system based on digital elevation data. We proved that volcano-tectonic deformation alters surface morphology distinctly enough to produce drainage divides (topographic highs) by using this method to delineate the well-known boundaries of Mt. Etna and Kilauea. This method can be easily applied to delineate potential boundaries of unstable flanks at other volcanoes.

CRediT authorship contribution statement

Luisa Rollwage: Writing – original draft, Visualization, Methodology, Investigation, Conceptualization. **Olga Sánchez-Guillamón:** Writing – review & editing, Project administration, Investigation. **Christian Sippl:** Writing – original draft, Visualization, Methodology, Investigation. **Ricardo León:** Writing – review & editing, Investigation. **Juan Tomás Vázquez:** Writing – review & editing, Investigation. **Morelia Urlaub:** Writing – review & editing, Investigation. **Felix Gross:** Writing – review & editing, Investigation. **Christoph Böttner:** Writing – review & editing, Investigation. **Sebastian Krastel:** Writing – review & editing, Supervision, Project administration. **Jacob Geersen:** Writing – original draft, Supervision, Methodology, Investigation, Conceptualization.

Declaration of competing interest

The authors declare that they have no known competing financial interests or personal relationships that could have appeared to influence the work reported in this paper.

Data availability

The raw EM122 multibeam data of the MSM113 cruise are achieved at Pangea (https://doi.pangaea.de/10.1594/PANGAEA.965107). The processed and gridded bathymetry and backscatter data sets will also be uploaded to Pangea https://pangaea.de/. The processed and gridded shallow multibeam data sets (EM710) from the Vulcana cruises will be available at the CSIC repository (DIGITAL CSIC; https://www.csic.es/en/open-science).

Acknowledgments

We thank the captain and crew of R/V Maria S. Merian for their professional support during cruise MSM113. We extend our sincere gratitude to the officers and crew of the R/V Ramón Margalef and Ángeles Alvariño from IEO-CSIC for their exceptional support during the time at sea during the volcanic eruption. Their dedication and expertise greatly contributed to the success of the Vulcana oceanographic surveys. The Spanish oceanographic cruises were supported by the Spanish Oceanographic Institute (IEO-CSIC) through the VULCANA-III project (IEO-CSIC-2021-2023) and the special fund of the Ministry of Science and Innovation of the Spanish Government (20223PAL005) related to La Palma 2021 volcanic eruption. Sincere thanks to Neil C. Mitchell, Daniele Casalbore and two anonymous reviewers for thorough reviews that helped improving the manuscript.

Funding

This research did not receive any specific grant from funding agencies in the public, commercial, or not-for-profit sectors.

References

Acosta, J., Uchupi, E., Smith, D., Muñoz, A., Herranz, P., Palomo, C., Llanes, P., Ballesteros, M., ZEE Working Group, 2005. Comparison of Volcanic Rifts on La Palma and El Hierro, Canary Islands and the Island of Hawaii. Geophysics of the Canary Islands: Results of Spain's Exclusive Economic Zone Program, pp. 59–90.

Ancochea, E., Hernán, F., Cendrero, A., Cantagrel, J.M., Fúster, J., Ibarrola, E., Coello, J., 1994. Constructive and destructive episodes in the building of a young oceanic island, La Palma, Canary Islands, and genesis of the Caldera de Taburiente. J. Volcanol. Geotherm. Res. 60 (3–4), 243–262.

Azzaro, R., Bonforte, A., Branca, S., Guglielmino, F., 2013. Geometry and kinematics of the fault systems controlling the unstable flank of Etna volcano (Sicily). J. Volcanol. Geotherm. Res. 251, 5–15.

Becker, J.J., Sandwell, D.T., Smith, W.H.F., Braud, J., Binder, B., Depner, J.L., Fabre, D., Factor, J., Ingalls, S., Kim, S.-H., Ladner, R., Marks, K., Nelson, S., Pharaoh, A., Trimmer, R., Von Rosenberg, J., Wallace, G., Weatherall, P., 2009. Global bathymetry and elevation data at 30 arc seconds resolution: SRTM30_PLUS. Mar. Geod. 32 (4), 355–371.

Cabrera-Pérez, I., Soubestre, J., D'Auria, L., Barrancos, J., Martín-Lorenzo, A., van Dorth, D.M., Padilla, G.D., Przeor, M., Pérez, N.M., 2023. Geothermal and structural features of La Palma island (Canary Islands) imaged by ambient noise tomography. Sci. Rep. 13 (1), 12892.

Camacho, A.G., Fernández, J., González, P.J., Rundle, J.B., Prieto, J.F., Arjona, A., 2009. Structural results for La Palma island using 3-D gravity inversion. J. Geophys. Res. Solid Earth 114 (B5).

Carracedo, J.C., 1994. The Canary Islands: an example of structural control on the growth of large oceanic-island volcanoes. J. Volcanol. Geotherm. Res. 60 (3–4), 225–241.

Carracedo, J.C., Day, S.J., Guillou, H., Gravestock, P., 1999a. Later stages of volcanic evolution of La Palma, Canary Islands: rift evolution, giant landslides, and the genesis of the Caldera de Taburiente. Geol. Soc. Am. Bull. 111 (5), 755–768.

Carracedo, J.C., Day, S.J., Guillou, H., Torrado, F.J.P., 1999b. Giant quaternary landslides in the evolution of La Palma and El Hierro, Canary Islands. J. Volcanol. Geotherm. Res. 94 (1–4), 169–190.

Carracedo, J.C., Badiola, E.R., Guillou, H., de La Nuez, J., Torrado, F.P., 2001. Geology and volcanology of la Palma and el Hierro, western Canaries. Estud. Geol.-Madrid 57, 175–273.

Carracedo, J.C., Guillou, H., Badiola, E.R., Cueto-Pascual, L.A., 2015. El Pueblo. Hoja 1085III/IV. Mapa Geologico de España Escala 1:25.000. Instituto Geológico y Minero de España. ISBN: 978-84-7840-976-1.

Carracedo, J.C., Troll, V.R., Day, J.M., Geiger, H., Aulinas, M., Soler, V., Deegan, F.M., Perez-Torrado, F.J., Gisbert, G., Gazel, E., Rodriguez-Gonzalez, A., Albert, H., 2022. The 2021 eruption of the Cumbre Vieja volcanic ridge on La Palma, Canary Islands. Geol. Today 38 (3), 94–107.

Cervelli, P., Segall, P., Johnson, K., Lisowski, M., Miklius, A., 2002. Sudden aseismic fault slip on the south flank of Kilauea volcano. Nature 415 (6875), 1014–1018.

D'Auria, L., Koulakov, I., Prudencio, J., Cabrera-Pérez, I., Ibáñez, J.M., Barrancos, J., García-Hernández, R., van Dorth, D.M., Padilla, G.D., Przeor, M., Ortega, V., Hernández, P., Peréz, N.M., 2022. Rapid magma ascent beneath La Palma revealed by seismic tomography. Sci. Rep. 12, 17654.

D'Auria, L., Santos, A., Hernández, P.A., Melián, G.V., Álvarez Díaz, A.J., Asensio-Ramos, M., González Pérez, A.M., Pérez, N.M., 2023. Modeling outdoor dispersion of CO2 at Puerto Naos (La Palma, Canary Islands). In: EGU General Assembly Conference Abstracts (pp. EGU-3834) (May).

Day, S.J., Carracedo, J.C., Guillou, H., Gravestock, P., 1999. Recent structural evolution of the Cumbre Vieja volcano, La Palma, Canary Islands: volcanic rift zone reconfiguration as a precursor to volcano flank instability? J. Volcanol. Geotherm. Res. 94 (1–4), 135–167.

Dayton, K., Gazel, E., Wieser, P., Troll, V.R., Carracedo, J.C., La Madrid, H., Roman, D.C., Ward, J., Aulinas, M., Geiger, H., Deegan, F.M., Gisbert, G., Perez-Torrado, F.J., 2023. Deep magma storage during the 2021 La Palma eruption. Sci. Adv. 9 (6), eade7641.

Del Fresno, C., Cesca, S., Klügel, A., Domínguez Cerdeña, I., Díaz-Suárez, E.A., Dahm, T., García-Cañada, L., Meletlidis, S., Milkereit, C., Valenzuela-Malebrán, C., López-Díaz, R., López, C., 2023. Magmatic plumbing and dynamic evolution of the 2021 La Palma eruption. Nat. Commun. 14 (1), 358.

Del Potro, R., Hürlimann, M., 2009. The decrease in the shear strength of volcanic materials with argillic hydrothermal alteration, insights from the summit region of Teide stratovolcano, Tenerife. Eng. Geol. 104 (1–2), 135–143.

Denlinger, R.P., Morgan, J.K., 2014. Instability of Hawaiian volcanoes. In: Characteristics of Hawaiian Volcanoes, 1801, pp. 149–176.

Denlinger, R.P., Okubo, P., 1995. Structure of the mobile south flank of Kilauea Volcano, Hawaii. J. Geophys. Res. Solid Earth 100 (B12), 24499–24507.
Fernández, J., Escayo, J., Hu, Z., Camacho, A.G., Samsonov, S.V., Prieto, J.F., Tiampo, K. F., Palano, M., Mallorquí, J.J., Ancochea, E., 2021. Detection of volcanic unrest onset in La Palma, Canary Islands, evolution and implications. Sci. Rep. 11 (1), 2540.
Fernández, J., Escayo, J., Camacho, A.G., Palano, M., Prieto, J.F., Hu, Z., Samsonov, S.V., Tiampo, K.F., Ancochea, E., 2022. Shallow magmatic intrusion evolution below La Palma before and during the 2021 eruption. Sci. Rep. 12 (1), 20257.
Fraile-Nuez, E., Santana-Casiano, J.M., Fernández-Salas, L.M., Sánchez-Guillamón, O., Presas-Navarro, C., Santana-González, C., García, O., Cosme, M., Alduán, M., Lozano, E., García-Talavera, F., Iribarren, I., Domínguez-Yanes, J.F., 2015. Informe científico-técnico de la campaña Vulcana-1015. Instituto Español de Oceanografía, 17 p.
Fraile-Nuez, E., Vázquez, J.T., Gómez-Ballesteros, M., Sánchez, O., Naranjo, S., Ferrera, I., Arrieta, J.M., Huertas, E., Tovar, A., Roque, D., Navarro, G., Galindo, I., Mata, P., Rodríguez, A., Machín, F., Hernández-Guerra, S., Álvarez-Valero, A., Lozano, E., Presas-Navarro, C., Escanez, J., González-Vega, A., Martín-Díaz, J.P., 2021a. Resultados preliminares sobre la presencia de anomalías físico-químicas y biológicas en el océano circundante al delta de lava de la erupción de CumbreVieja en la isla de La Palma. Campaña Vulcana-III-0921-LP. Instituto Español de Oceanografía, CSIC, 17 p.
Fraile-Nuez, E., Vázquez, J.T., Gómez-Ballesteros, M., Sánchez, O., Naranjo, S., Ferrera, I., Arrieta, J.M., Huertas, E., Tovar, A., Roque, D., Navarro, G., Galindo, I., Mata, P., Rodríguez, A., Machín, F., Hernández-Guerra, S., Álvarez-Valero, A., Lozano, E., Presas-Navarro, C., Escanez, J., González-Vega, A., Martín-Díaz, J.P., 2021b. Resultados preliminares sobre la presencia deanomalías físico-químicas y biológicas en el océanocircundante al delta de lava de la erupción de CumbreVieja en la isla de La Palma. Campaña Vulcana-III-1021-LP. Instituto Español de Oceanografía, CSIC, 16 p.
Furst, S., Urlaub, M., Klein, E., Bonanati, C., 2023. Are eruptions reliable precursors to marine volcano collapses? Front. Earth Sci. 11. Art-Nr.
González, P.J., 2022. Volcano-tectonic control of Cumbre Vieja. Science 375 (6587), 1348–1349.
González, P.J., Tiampo, K.F., Camacho, A.G., Fernández, J., 2010. Shallow flank deformation at Cumbre Vieja volcano (Canary Islands): implications on the stability of steep-sided volcano flanks at oceanic islands. Earth Planet. Sci. Lett. 297 (3–4), 545–557.
Gross, F., Krastel, S., Geersen, J., Behrmann, J.H., Ridente, D., Chiocci, F.L., Bialas, J., Papenberg, C., Cukur, D., Urlaub, M., Micallef, A., 2016. The limits of seaward spreading and slope instability at the continental margin offshore Mt Etna, imaged by high-resolution 2D seismic data. Tectonophysics 667, 63–76.
Guillou, H., Carracedo, J.C., Day, S.J., 1998. Dating of the upper Pleistocene–Holocene volcanic activity of La Palma using the unspiked K–Ar technique. J. Volcanol. Geotherm. Res. 86 (1–4), 137–149.
Gutscher, M.A., Kopp, H., Krastel, S., Bohrmann, G., Garlan, T., Zaragosi, S., Klaucke, I., Wintersteller, P., Loubrieu, B., Le Faou, Y., San Pedro, L., Dominguez, S., Rovere, M., de Lepinay, B.M., Ranero, C., Sallares, V., 2017. Active tectonics of the Calabrian subduction revealed by new multi-beam bathymetric data and high-resolution seismic profiles in the Ionian Sea (Central Mediterranean). Earth Planet. Sci. Lett. 461, 61–72.
Heap, M.J., Baumann, T., Gilg, H.A., Kolzenburg, S., Ryan, A.G., Villeneuve, M., Russell, J.K., Kennedy, L.A., Rosas-Carbajal, M., Clynne, M.A., 2021. Hydrothermal alteration can result in pore pressurization and volcano instability. Geology 49 (11), 1348–1352.
Hernández, P.A., Salazar, J.M., Shimoike, Y., Mori, T., Notsu, K., Pérez, N., 2001. Diffuse emission of CO2 from Miyakejima volcano, Japan. Chem. Geol. 177 (1–2), 175–185.
Hildenbrand, A., Gillot, P.Y., Soler, V., Lahitte, P., 2003. Evidence for a persistent uplifting of La Palma (Canary Islands), inferred from morphological and radiometric data. Earth Planet. Sci. Lett. 210 (1–2), 277–289.
Hunt, J.A., Pyle, D.M., Mather, T.A., 2019. The geomorphology, structure, and lava flow dynamics of peralkaline rift volcanoes from high-resolution digital elevation models. Geochem. Geophys. Geosyst. 20 (3), 1508–1538.
Karstens, J., Crutchley, G.J., Hansteen, T.H., Preine, J., Carey, S., Elger, J., Kühn, M., Nomikou, P., Schmid, F., Dalla Valle, G., Kelfoun, K., Berndt, C., 2023. Cascading events during the 1650 tsunamigenic eruption of Kolumbo volcano. Nat. Commun. 14 (1), 6606.
Klein, E., Hadré, E., Krastel, S., Urlaub, M., 2023. An evaluation of the General Bathymetric Chart of the Ocean in shoreline-crossing geomorphometric investigations of volcanic islands. Front. Mar. Sci. 10. Art-Nr.
Krastel, S., Cruise Participants, 2024. R/V Maria S. Merian Cruise Report MSM 113, Las Palmas (Spain) – Las Palmas – Las Palmas (Spain), 09.12. – 12.01.23.
Krastel, S., Schmincke, H.U., Jacobs, C.L., Rihm, R., Le Bas, T.P., Alibés, B., 2001. Submarine landslides around the Canary Islands. J. Geophys. Res. Solid Earth 106 (B3), 3977–3997.
Lin, G., Okubo, P.G., 2020. Seismic evidence for a shallow detachment beneath Kīlauea's south flank during the 2018 activity. Geophys. Res. Lett. 47 (15), e2020GL088003.
Liu, C., Lay, T., Xiong, X., 2018. MW 6.9 earthquake seaward of the Kilauea east rift zone fissure eruption in Hawaii. Geophys. Res. Lett. 45 (18), 9508–9515.
Maccaferri, F., Smittarello, D., Pinel, V., Cayol, V., 2019. On the propagation path of magma-filled dikes and hydrofractures: the competition between external stress, internal pressure, and crack length. Geochem. Geophys. Geosyst. 20 (4), 2064–2081.
Masson, D.G., Watts, A.B., Gee, M.J.R., Urgeles, R., Mitchell, N.C., Le Bas, T.P., Canals, M., 2002. Slope failures on the flanks of the western Canary Islands. Earth Sci. Rev. 57 (1–2), 1–35.
Menand, T., Daniels, K.A., Benghiat, P., 2010. Dyke propagation and sill formation in a compressive tectonic environment. J. Geophys. Res. Solid Earth 115 (B8).
Micallef, A., Berndt, C., Masson, D.G., Stow, D.A., 2007. A technique for the morphological characterization of submarine landscapes as exemplified by debris flows of the Storegga Slide. J. Geophys. Res. Earth 112 (F2).
Mitchell, N.C., Masson, D.G., Watts, A.B., Gee, M.J., Urgeles, R., 2002. The morphology of the submarine flanks of volcanic ocean islands: a comparative study of the Canary and Hawaiian hotspot islands. J. Volcanol. Geotherm. Res. 115 (1–2), 83–107.
Mitchell, N.C., Quartau, R., Madeira, J., 2012. Assessing landslide movements in volcanic islands using near-shore marine geophysical data: south Pico island, Azores. Bull. Volcanol. 74, 483–496.
Morgan, J.K., Moore, G.F., Hills, D.J., Leslie, S., 2000. Overthrusting and sediment accretion along Kilauea's mobile south flank, Hawaii: evidence for volcanic spreading from marine seismic reflection data. Geology 28 (7), 667–670.
Morgan, J.K., Moore, G.F., Clague, D.A., 2003. Slope failure and volcanic spreading along the submarine south flank of Kilauea volcano, Hawaii. J. Geophys. Res. Solid Earth 108 (B9).
Ohsawa, S., Kazahaya, K., Yasuhara, M., Kono, T., Kitaoka, K., Yusa, Y., Yamaguchi, K., 2002. Escape of volcanic gas into shallow groundwater systems at Unzen Volcano (Japan): evidence from chemical and stable carbon isotope compositions of dissolved inorganic carbon. Limnology 3, 0169–0173.
Owen, S., Segall, P., Lisowski, M., Miklius, A., Denlinger, R., Sako, M., 2000. Rapid deformation of Kilauea Volcano: global positioning system measurements between 1990 and 1996. J. Geophys. Res. Solid Earth 105 (B8), 18983–18998.
Padrón, E., Pérez, N.M., Rodríguez, F., Melián, G., Hernández, P.A., Sumino, H., Padilla, G., Barrancos, J., Dionis, S., Notsu, K., Calvo, D., 2015. Dynamics of diffuse carbon dioxide emissions from Cumbre Vieja volcano, La Palma, Canary Islands. Bull. Volcanol. 77, 1–15.
Palano, M., Sparacino, F., Gambino, P., D'Agostino, N., Calcaterra, S., 2022. Slow slip events and flank instability at Mt. Etna volcano (Italy). Tectonophysics 836, 229414.
Paris, R., 2015. Source mechanisms of volcanic tsunamis. Philos. Trans. R. Soc. A Math. Phys. Eng. Sci. 373 (2053), 20140380.
Phillips, K.A., Chadwell, C.D., Hildebrand, J.A., 2008. Vertical deformation measurements on the submerged south flank of Kīlauea volcano, Hawai'i reveal seafloor motion associated with volcanic collapse. J. Geophys. Res. Solid Earth 113 (B5).
Pinel, V., Furst, S., Maccaferri, F., Smittarello, D., 2022. Buoyancy versus local stress field control on the velocity of magma propagation: insight from analog and numerical modelling. Front. Earth Sci. 10, 838318.
Poland, M.P., Peltier, A., Bonforte, A., Puglisi, G., 2017. The spectrum of persistent volcanic flank instability: a review and proposed framework based on Kīlauea, Piton de la Fournaise, and Etna. J. Volcanol. Geotherm. Res. 339, 63–80.
Quartau, R., Trenhaile, A.S., Mitchell, N.C., Tempera, F., 2010. Development of volcanic insular shelves: insights from observations and modelling of Faial Island in the Azores Archipelago. Mar. Geol. 275 (1–4), 66–83.
Quartau, R., Madeira, J., Mitchell, N.C., Tempera, F., Silva, P.F., Brandão, F., 2015. The insular shelves of the Faial-Pico Ridge (Azores archipelago): A morphological record of its evolution. Geochem. Geophys. Geosyst. 16 (5), 1401–1420.
Rodríguez-Pascua, M.Á., Perez-Lopez, R., Perucha, M.Á., Sánchez, N., López-Gutierrez, J., Mediato, J.F., Sanz-Mangas, D., Lozano, G., Galindo, I., García-Davalillo, D., Carnicero, C.L., Béjar, M., 2024. Active Faults, Kinematics, and Seismotectonic Evolution during Tajogaite Eruption 2021 (La Palma, Canary Islands, Spain). Appl. Sci. 14 (7), 2745.
Ryan, W.B., Carbotte, S.M., Coplan, J.O., O'Hara, S., Melkonian, A., Arko, R., Weissel, R. A., Ferrini, V., Goodwillie, A., Nitsche, F., Bonczkowski, J., Zemsky, R., 2009. Global multi-resolution topography synthesis. Geochem. Geophys. Geosyst. 10 (3).
Schaefer, L.N., Di Traglia, F., Chaussard, E., Lu, Z., Nolesini, T., Casagli, N., 2019. Monitoring volcano slope instability with Synthetic Aperture Radar: a review and new data from Pacaya (Guatemala) and Stromboli (Italy) volcanoes. Earth Sci. Rev. 192, 236–257.
Staudigel, H., Feraud, G., Giannerini, G., 1986. The history of intrusive activity on the island of La Palma (Canary Islands). J. Volcanol. Geotherm. Res. 27 (3–4), 299–322.
Thiele, S.T., Cruden, A.R., Micklethwaite, S., 2023. Failure of load-bearing dyke networks as a trigger for volcanic edifice collapse. Commun. Earth Environ. 4 (1), 382.
Urgeles, R., Canals, M., Baraza, J., Alonso, B., Masson, D., 1997. The most recent megalandslides of the Canary Islands: El Golfo debris avalanche and Canary debris flow, west El Hierro Island. J. Geophys. Res. Solid Earth 102 (B9), 20305–20323.
Urgeles, R., Masson, D.G., Canals, M., Watts, A.B., Le Bas, T., 1999. Recurrent large-scale landsliding on the west flank of La Palma, Canary Islands. J. Geophys. Res. Solid Earth 104 (B11), 25331–25348.
Urlaub, M., Geersen, J., Petersen, F., Gross, F., Bonforte, A., Krastel, S., Kopp, H., 2022. The submarine boundaries of Mount Etna's unstable southeastern flank. Front. Earth Sci. 10, 810790.
Walter, T., Schmincke, H.U., 2002. Rifting, recurrent landsliding and Miocene structural reorganization on NW-Tenerife (Canary Islands). Int. J. Earth Sci. 91, 615–628.
Walter, T.R., Haghshenas Haghighi, M., Schneider, F.M., Coppola, D., Motagh, M., Saul, J., Babeyko, A., Dahm, T., Troll, V.R., Tilmann, F., Heimann, S., Valade, S., Triyono, R., Khomarudin, R., Kartadinata, N., Laiolo, M., Massimetti, F., Gaebler, P., 2019. Complex hazard cascade culminating in the Anak Krakatau sector collapse. Nat. Commun. 10 (1), 4339.
Watanabe, T., Masuyama, T., Nagaoka, K., Tahara, T., 2002. Analog experiments on magma-filled cracks competition between external stresses and internal pressure. Earth Planets Space 54 (12), 1247–1261.
Wei, X., Shen, Y., Caplan-Auerbach, J., Morgan, J.K., 2021. An OBS array to investigate offshore seismicity during the 2018 Kīlauea eruption. In: Seismological Society of America, 92(1), pp. 603–612.